

# Domain Generalization in LiDAR Semantic Segmentation Leveraged by Density Discriminative Feature Embedding

Jaeyul Kim, Jungwan Woo, Jeonghoon Kim, and Sunghoon Im

**Abstract**—While significant progress has been achieved in LiDAR-based perception, domain generalization continues to present challenges, often resulting in reduced performance when encountering unfamiliar datasets due to domain discrepancies. One of the primary hurdles stems from the variability of LiDAR sensors, leading to inconsistencies in point cloud density distribution. Such inconsistencies can undermine the effectiveness of perception models. We address this challenge by introducing a new approach that acknowledges a fundamental characteristic of LiDAR: the variation in point density due to the distance from the LiDAR to the scene, and the number of beams relative to the field of view. Understanding this, we view each LiDAR’s point cloud at various distances as having distinct density distributions, which can be consistent across different LiDAR models. With this insight, we propose the Density Discriminative Feature Embedding (DDFE) module, crafted to specifically extract features related to density while ensuring domain invariance across different LiDAR sensors. In addition, we introduce a straightforward but effective density augmentation technique, designed to broaden the density spectrum and enhance the capabilities of the DDFE. The proposed DDFE stands out as a versatile and lightweight domain generalization module. It can be seamlessly integrated into various 3D backbone networks, consistently outperforming existing state-of-the-art domain generalization approaches. We commit to releasing the source code publicly to foster community collaboration and advancement.

**Index Terms**—Autonomous vehicles, 3D semantic segmentation, Domain Generalization, 3D LiDAR.

## I. INTRODUCTION

**L**IGHT Detection and Ranging (LiDAR) provides detailed 3D data, making it indispensable for environmental perception in autonomous vehicles. Among the various LiDAR-based perception tasks, semantic segmentation plays a crucial role in understanding the driving scene by classifying each point into multiple classes. While LiDAR-based semantic segmentation [1]–[3] have been widely studied, their impressive performance is often constrained to scenarios where source and target datasets align perfectly. However, mismatches between these datasets can lead to significant performance declines. These are mainly attributed to two primary factors: variations in the environment — illustrated by datasets Waymo in the USA [4], KITTI in the Germany [5], and nuScenes in the Singapore [6] — and sensor-induced discrepancies in the

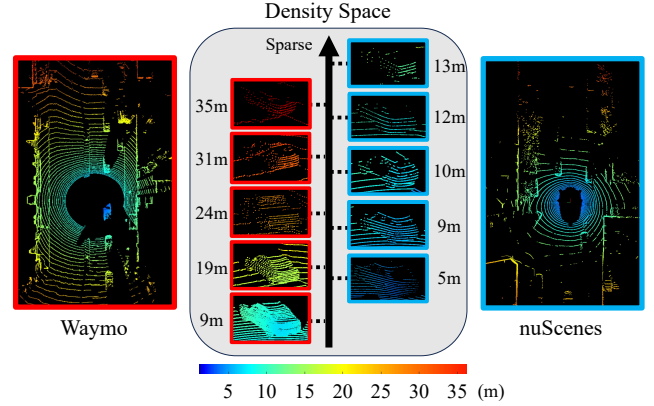


Fig. 1: Illustration of our motivation that, despite the distinct density distributions between the Waymo dataset (64-channel) and the nuScenes dataset (32-channel), overlapping density distributions still exist between these datasets.

number of beams and Field of View (FoV). Numerous unsupervised domain adaptation studies [7]–[9] offer solutions but demand separate fine-tuning before deployment. In contrast, models trained with robust domain generalization methods hold greater promise for real-time autonomous driving systems. However, the crucial field remains under-researched and its potential is yet to be fully realized. Existing study [10] has pinpointed the point cloud density distribution as a prime performance hindrance. While some solutions like point cloud sampling and completion-based methods attempt to remedy this, they fall short in achieving the desired performance [11] and require sequentially labeled data and knowledge of ego-motion [12].

In this paper, we introduce a new perspective in domain generalization, focusing on the challenges posed by density variations from different LiDAR sensors. Previous research [10], [13], [14] primarily concentrated on global density differences, typically considering datasets from 64-channel LiDARs like Waymo [4] denser than those from 32-channel LiDARs like nuScenes [6]. However, as shown in Fig. 1, density comparisons can be more nuanced. For example, a vehicle at 9 meters in Waymo appears denser than one at the same distance in nuScenes, but at different distances, such as a vehicle at 35 meters in Waymo versus 9 meters in nuScenes, the latter may appear denser. This inconsistency arises from an inherent property of LiDAR sensors where density varies with distance. Recognizing this, we view each LiDAR’s point cloud

The authors are with the Department of Electrical Engineering and Computer Science, DGIST, Daegu 42988, Republic of Korea (e-mail: {jykim94, friendship1, jeonghoon, sunghoonim}@dgist.ac.kr). Jaeyul Kim and Jungwan Woo contributed equally to this work (Corresponding author: Sunghoon Im).

at various distances as having distinct density distributions, which can be consistent across different LiDAR models. This implies that despite the resolution differences in LiDAR sensors, overlapping density domains can exist within these multiple domains. For example, vehicles at certain distances in Waymo and nuScenes could have similar densities. This understanding of overlapping density domains provides vital insights for domain generalization.

Building on these observations, we present a domain alignment method expertly, tailored to both discern and enhance shared density distributions. We hypothesize that even if the density distributions of source and unseen data differ, there may still be overlapping density regions between them. At the core of our strategy is the density-aware embedding module that modulates features by utilizing attention metrics, guided by our beam density estimation. The beam density estimation module is designed to encode the density inherent to each 3D voxel, facilitating a detailed differentiation of densities specific to certain regions. Furthermore, we introduce a density soft clipping technique. This method constrains the density spectrum, ensuring it does not encompass density distributions from unseen domains that are absent in source datasets. To supplement this, we use density augmentation to widen the density spectrum of the source data, thereby enhancing its domain generalization capabilities. Extensive experiments validate the superiority of our method over the conventional domain adaptation and generalization methods across multiple 3D backbone networks.

In summary, our primary contributions include:

- We introduce a new perspective for domain generalization to overcome density variations caused by different LiDAR sensors, utilizing the characteristic of LiDAR where density varies with distance.
- We propose a density discriminative feature embedding module, DDFE, designed to identify shared density distribution and subsequently amplify relevant features.
- We present a simple yet effective data augmentation strategy, aimed at broadening the density spectrum of source data.
- Extensive experiments demonstrate that our method outperforms state-of-the-art Domain Generalization (DG), as well as Domain Adaptation (DA) approaches.

## II. RELATED WORK

### A. LiDAR-based Semantic Segmentation

LiDAR point clouds pose unique challenges due to their irregular, unordered, and unstructured nature, making standard image-based convolution operations inapplicable. Research on representing point cloud data can be broadly categorized into Projection-based, point-based, and voxel-based method. Projection-based methods transform a 3D point cloud into a 2D range view through either a spherical or bird’s-eye view projection. By doing so, they can utilize lightweight models like 2D convolution [15]–[18] or transformer [3], [19] rather than 3D convolution. Nevertheless, such methods face the inherent limitation of 2D kernels not preserving the receptive field in the actual 3D space. Point-based methods [20]–[22]

directly extract features from the point cloud. These methods utilize all the 3D spatial information without distortion. However, the trade-off is a substantial demand on memory and computational resources. In voxel-based approaches, point clouds are segmented into 3D grids, known as voxels, and features are extracted using 3D convolutional methods. However, the high computational and memory demands of dense 3D convolution have prompted recent research [1], [2], [23], [24] to adopt sparse 3D convolution techniques. Furthermore, studies [1], [2] have employed cylindrical partitioning techniques to effectively manage the challenges posed by uneven and imbalanced density distributions that occur at varying distances.

### B. LiDAR-based Domain Adaptation

Differences in the LiDAR sensor or changes in the operating environment induce variations in the distribution of point cloud data. These variations can subsequently compromise the perception performance of autonomous driving systems. Constructing training datasets for every individual sensor and location to mitigate this degradation in performance is prohibitively expensive. In the quest for cost-effective performance maintenance, the spotlight has shifted towards unsupervised domain adaptation [7], [9], [25]–[27]. This strategy aims to leverage both the labeled source datasets and unlabeled target datasets to maintain the performance in the target domain. Yi *et al.* [11] leverage sequential LiDAR frame data to train a network that reconstructs dense frames, performing semantic segmentation in a canonical domain for adaptation. Saltori *et al.* [28] propose a source-free unsupervised domain adaptation (SF-UDA) strategy for 3D object detection, allowing model adaptation to target datasets without source dataset reference. Rochan *et al.* [29] propose a range view-based unsupervised domain adaptation method, aligning beam positions between training and target data, thereby ensuring spatial consistency in sensor data for model adaptation. Yuan *et al.* [8] present a multi-scale feature extraction technique to handle LiDAR density variations and propose an adversarial learning weight mechanism, capitalizing on consistency in class predictions across point and voxel representations. Shaban *et al.* [30] introduce LiDAR-UDA, combining point cloud subsampling to mimic various LiDAR types and refining pseudo labels through Cross-frame Ensembling and a Learned Aggregation Model (LAM). Although these domain adaptation methods demonstrate effectiveness, they share a common limitation: the need for individual fine-tuning with target data upon each domain shift.

### C. LiDAR-based Domain Generalization

Domain Generalization aims to improve the performance in scenarios where the target domain data, unseen during training, is encountered. Research on domain generalization for LiDAR-based perception has recently witnessed a surge, as highlighted in a number of studies [10], [12], [31]–[35]. Kim *et al.* [10] emphasize generalizable representation learning. Their method leverages sparsity invariance feature consistency and bridges the semantic correlation consistency between

TABLE I: LiDAR configuration for each dataset.

	Waymo	SemanticKITTI	nuScenes
$H_{\text{beam}}$	2560	2048	1080
$V_{\text{beam}}$	64	64	32
$[f_{\min}, f_{\max}]$ ( $^{\circ}$ )	$[-17.6, +2.4]$	$[-24.8, +2.0]$	$[-30.0, +10.0]$

the source data and the sparse domain generated by beam sampling. Ryu *et al.* [12] introduce a method to aggregate multiple frames to generate dense world models and augment data by sampling through randomized LiDAR configurations. However, this approach is limited in requiring knowledge of ego-motion and the sequentially labeled data. Li *et al.* [34] introduce BEV-DG to improve domain generalization in cross-modal semantic segmentation. They employ a bird’s-eye view for enhanced cross-modal learning and develop Density-maintained Vector Modeling (DVM) for efficient learning of domain-invariant features. Saltori *et al.* [35] explore domain generalization in LiDAR semantic segmentation, using both synthetic and real-world datasets. Their approach, LiDOG, utilizes semantic priors in a 2D bird’s-eye view to extract domain-agnostic features. Sanchez *et al.* [33] propose a label propagation approach incorporating multi-frame aggregation with known ego-motion. Nevertheless, this method is limited when the ego-motion is unknown and cannot run in real-time because it is based on KPConv [20], which is computationally expensive. Distinctively, our approach advances a single-frame domain generalization approach that considers the inherent characteristics of LiDAR. Consequently, our method offers the distinct advantage of bypassing the need for ego-motion and sequentially labeled data during the training and inference phases.

### III. METHOD

In this section, we introduce a domain generalization method for LiDAR semantic segmentation that leverages the unique characteristics of each LiDAR sensor, as shown in Tab. I and Fig. 2. First, we describe our point-voxel feature encoding network, adept at processing LiDAR point clouds by utilizing the capabilities of both point and voxel features. Subsequently, we detail our density embedding technique, designed to compute the expected density for each ray and modulate the encoded features to ensure generalization across different domains. Lastly, we introduce a simple yet effective data augmentation technique that extends the density range without the need for additional data, such as ego-motion or sequentially labeled data. The overall framework is shown in Fig. 3.

#### A. Point-voxel feature encoding

We introduce a technique to extract generalized representations across domains from point clouds. The distribution of intensity values varies depending on the LiDAR sensor. Leveraging intensity information can decrease the performance of perception models when transitioning between sensors. Thus, we omit the use of LiDAR intensity values to enhance domain generalization performance. Furthermore, each LiDAR sensor has a unique distribution of measurement

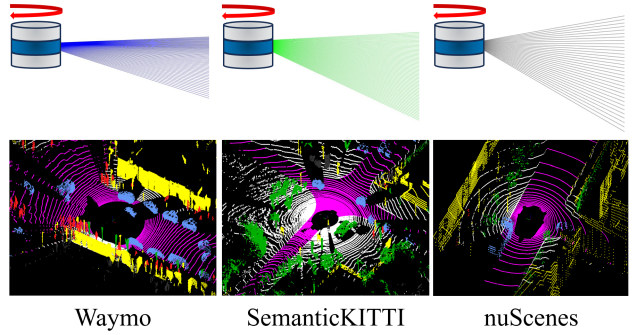


Fig. 2: Comparison of three different LiDAR datasets. Each dataset with its unique beam directions and corresponding point cloud shape.

errors, particularly within the intra-voxel region. To minimize variance induced by localized sensing noise, we incorporate a direct voxel-wise feature encoding into the PointNet-based feature extraction [36]. This direct encoding, which bypasses localized information within the voxels, effectively dismisses grid size variations, such as those of 20cm. Given a point cloud  $\mathbf{P} = \{p_i \in \mathbb{R}^3 \mid i = 1, \dots, N\}$  containing  $N$  3D points, we initially partition it into  $M$  3D voxels. For each voxel  $v_j$ , it is defined as a set of points and is represented by  $\mathbf{V} = \{v_j \in \mathbb{R}^{L \times 3} \mid j = 1, \dots, M\}$ , where  $L$  indicates the number of points contained in each voxel. The coordinates of these points are subsequently transformed into the form of  $(\cos(\theta_j), \sin(\theta_j), \phi_j, r_j)$ , where  $(\theta_j, \phi_j, r_j)$  correspond to spherical coordinates. These transformed coordinates are then encoded into voxel-wise features  $F^v \in \mathbb{R}^{M \times 16}$  through an MLP. We also encode point-wise features  $F^p \in \mathbb{R}^{N \times 16}$ , which are essential to produce point-wise outputs. For each point  $k$  in voxel  $v_j$  centered at  $(x_j^c, y_j^c, z_j^c)$ , we compute the offset as  $(x_{jk} - x_j^c, y_{jk} - y_j^c, z_{jk} - z_j^c)$ , with  $k = 1, \dots, L_j$ . Here,  $L_j$  represents the number of points belonging to  $v_j$ . These offsets are then processed by a point head to generate point-wise features.

#### B. Beam density estimation module

In this section, we detail the method to compute the density expectation for each ray emanating from a LiDAR sensor. Since all rays from a LiDAR originate from a singular source and are emitted at a fixed angle, the density associated with each beam can be deduced using a spherical projection informed by the beam configuration. The LiDAR sensor configuration, accessible from low-level sources such as an SDK, determines the set of horizontal and vertical inclinations  $\mathbf{C}_h$  and  $\mathbf{C}_v$  for each beam in this manner:

$$\begin{aligned} \mathbf{C}_h &= \left\{ \frac{2\pi}{H_{\text{beam}}} i \mid i \in \{1, \dots, H_{\text{beam}}\} \right\}, \\ \mathbf{C}_v &= \left\{ \frac{f_{\max} - f_{\min}}{V_{\text{beam}}} j + f_{\min} \mid j \in \{1, \dots, V_{\text{beam}}\} \right\}, \end{aligned} \quad (1)$$

where  $f_{\min}$  and  $f_{\max}$  denote the minimum and maximum LiDAR field of view, while  $H_{\text{beam}}$  and  $V_{\text{beam}}$  represent the number of horizontal and vertical beams, detailed in Tab. I.

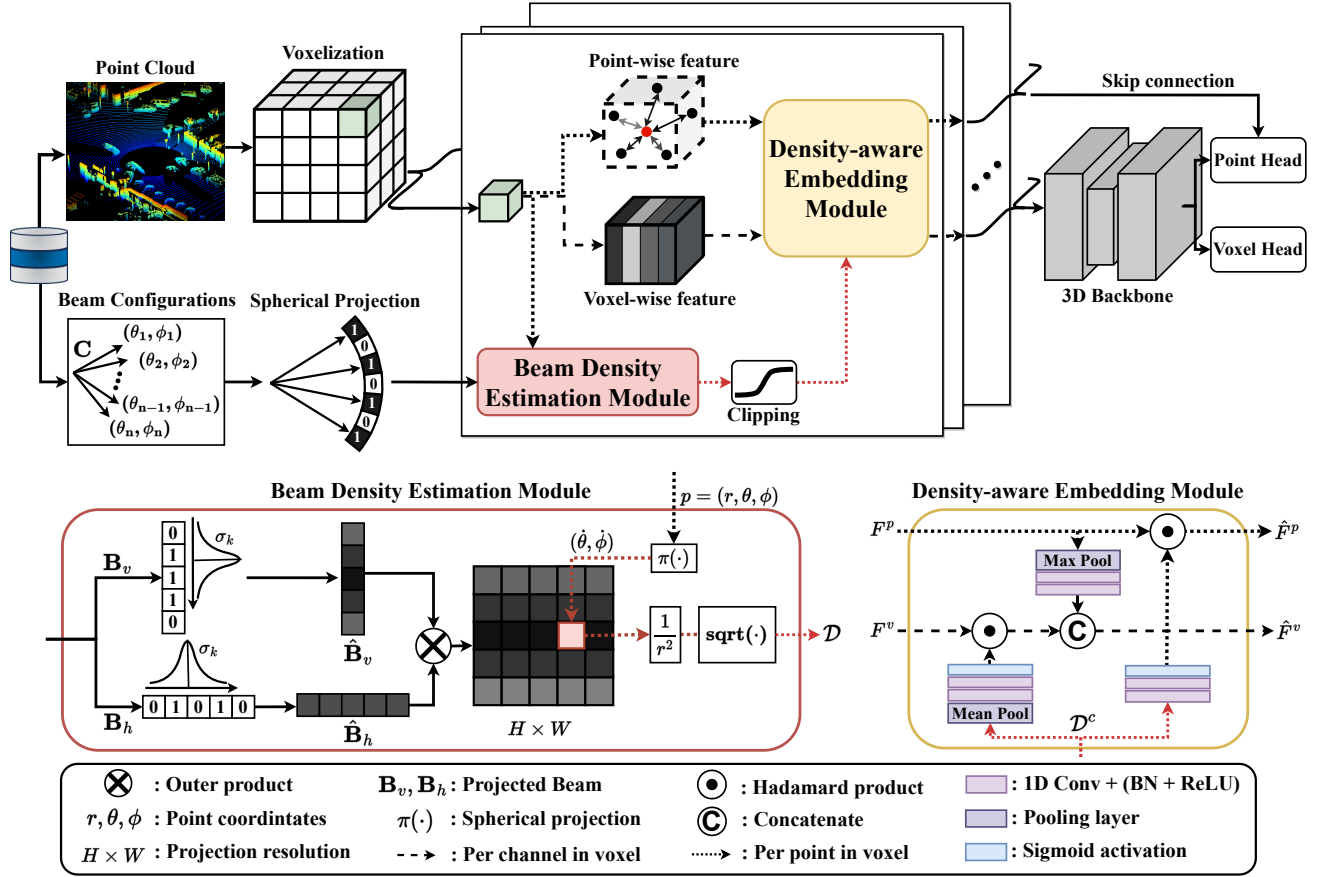


Fig. 3: Overview of the DDFE pipeline.

To project LiDAR beam inclinations onto spherical projected image coordinates, we use the projection function  $\pi : (\theta, \phi) \rightarrow (\dot{\theta}, \dot{\phi})$  defined as:

$$\dot{\theta} = \left\lfloor \frac{\theta}{2\pi} W \right\rfloor, \quad \dot{\phi} = \left\lfloor \frac{\phi - f_{\min}^{\text{proj}}}{f_{\max}^{\text{proj}} - f_{\min}^{\text{proj}}} H \right\rfloor, \quad (2)$$

where  $H$  and  $W$  are the height and width resolutions of the projected image, respectively set to  $H = 512$ ,  $W = 5120$ . We define the projected image's field of view as  $[f_{\min}^{\text{proj}}, f_{\max}^{\text{proj}}] = [-30.0, 15.0]$  to accommodate a range of LiDAR sensors. Given this, beam configurations can be transformed into 1-D binary vectors  $\mathbf{B}_v \in \mathbb{R}^H$  and  $\mathbf{B}_h \in \mathbb{R}^W$  as follows:

$$\mathbf{B}_h(\dot{\theta}) = \mathbb{1}_{\mathbf{C}_h}(\theta), \quad \mathbf{B}_v(\dot{\phi}) = \mathbb{1}_{\mathbf{C}_v}(\phi), \quad (3)$$

where  $\mathbb{1}_{\mathbf{C}}(x) = \begin{cases} 1, & \text{if } x \in \mathbf{C} \\ 0, & \text{otherwise} \end{cases}$ ,

where the indicator function  $\mathbb{1}(\cdot)$  yields 1 when the azimuth or elevation  $(\theta, \phi)$  of a pixel  $(\dot{\theta}, \dot{\phi})$  corresponds to the beam inclinations specified in  $\mathbf{C}$  in Eq. 1. Here,  $\mathbf{C}$  can be either  $\mathbf{C}_h$  or  $\mathbf{C}_v$  that represent the locations of projected vertical and horizontal beams, respectively. To compute the beam density, we convolve the binary vectors  $\mathbf{B}_h$  and  $\mathbf{B}_v$ , with four distinct 1-D Gaussian kernels, each characterized by standard deviations  $\sigma_k = \{10, 30, 50, 70\}$  as follows:

$$\hat{\mathbf{B}}_h = \mathbf{B}_h * \mathbf{G}_{\sigma_k}, \quad \hat{\mathbf{B}}_v = \mathbf{B}_v * \mathbf{G}_{\sigma_k}. \quad (4)$$

Finally, we define beam density  $\mathcal{D}_i$  of point  $p_i$  as follows:

$$\mathcal{D}_i = \sqrt{\hat{\mathbf{B}}_h(\dot{\theta}_i) \cdot \hat{\mathbf{B}}_v(\dot{\phi}_i) / r_i^2}, \quad (5)$$

where  $r_i$  is the radial distance of a LiDAR point  $p_i$  in the spherical coordinates. Taking into account that the density of the beam diminishes in proportion to the square of the distance due to its radial emission, we incorporate the inverse of  $r^2$  in our computation. Moreover, if the LiDAR conducts uniform scans in the horizontal direction, the Gaussian filter of  $\hat{\mathbf{B}}_h$  would yield a constant value across all outputs. In this case, we substitute  $\hat{\mathbf{B}}_h$  with  $H_{\text{beam}}$  for computational efficiency.

### C. Density soft clipping

When exposed to densities that deviate from those present in the source dataset, the model is susceptible to performance degradation in an unseen domain. To alleviate this issue, we introduce a density soft clipping method that confines the density spectrum using the  $\tanh(\cdot)$  function as follows:

$$\mathcal{D}_i^c = \tanh\left(\frac{\mathcal{D}_i - m}{l}\right) l + m, \quad (6)$$

$$m = \frac{\mathcal{P}_{90}(\mathcal{D}) + \mathcal{P}_{10}(\mathcal{D})}{2}, \quad l = \frac{\mathcal{P}_{90}(\mathcal{D}) - \mathcal{P}_{10}(\mathcal{D})}{2},$$

where  $\mathcal{D}_i^c$  is clipped density of point  $p_i$ , and  $\mathcal{P}_{90}$  and  $\mathcal{P}_{10}$  are functions that extract 90<sup>th</sup> and 10<sup>th</sup> channel-wise percentile values from the density embedding of the training domain,



---

**Algorithm 1** Point cloud Reservoir Sampling Algorithm
 

---

```

1: Initialize  $\mathcal{R}[1, \dots, N]$ ,  $\hat{p} \leftarrow 0$ ,  $c \leftarrow 0$   $\triangleright$   $\mathcal{R}$  is the reservoir
   memory,  $\hat{p}$  is the estimated percentile,  $N$  is the max size
   of reservoir,  $c$  is the number of resets
2: for point cloud  $\mathcal{P}$  in  $\mathcal{S}$  do  $\triangleright$   $\mathcal{S}$  is the stream of training
   point cloud data
3:    $\mathcal{D} \leftarrow$  calculate density from point cloud  $\mathcal{P}$ 
4:    $\rho \leftarrow \frac{N}{k}$   $\triangleright$   $k$  is the number of points processed so far
5:    $s \leftarrow \min(N, \text{round}(\rho \times |\mathcal{D}|))$ 
6:   if  $s < 1$  then
7:      $s \leftarrow N$ 
8:      $k \leftarrow 0$   $\triangleright$  Reset the count of processed points
9:      $c \leftarrow c + 1$ 
10:     $p_{\text{curr}} \leftarrow$  Calculate percentile of  $\mathcal{R}$ 
11:     $\hat{p} \leftarrow \hat{p} + \frac{p_{\text{curr}} - \hat{p}}{c}$   $\triangleright$  Calculate Cumulative Moving
   Average
12:  end if
13:  Select  $s$  random points from  $\mathcal{D}$ 
14:  Replace  $\mathcal{R}$  with these points
15:   $k \leftarrow k + |\mathcal{D}|$ 
16:  if  $c = 0$  then  $\triangleright$  Exception for first loop
17:     $\hat{p} \leftarrow$  Calculate percentile of  $\mathcal{R}$ 
18:  end if
19:  ForwardModel( $\mathcal{P}$ ,  $\hat{p}$ )  $\triangleright$  Model forward with
   estimated percentile
20: end for

```

---

respectively. Employing these percentile values allows us to discount the outlier density values. To calculate the percentile on the fly under memory constraints, we adopt the Reservoir Sampling technique with a sample size  $N = 1000$ . A comprehensive description of the algorithm is provided in Alg. 1.

#### D. Density-aware embedding module

For each point  $p_i$ , we derive a point-wise density embedding feature  $\mathcal{D}_i^c$ , using the beam density estimation module with density soft clipping. This feature serves as an input of both a point-wise attention function  $f_p$  and a voxel-wise attention function  $f_v$ , facilitating the generation of the domain-invariant density-discriminative features. In the case of point-wise attention,  $\mathcal{D}_i^c$  is dimensionally aligned with the point-wise feature  $F_i^p$  to generate density discriminative feature  $\hat{F}_i^p$  as follows:

$$\hat{F}_i^p = f_p(\mathcal{D}_i^c) \odot F_i^p, \quad (7)$$

where  $f_p$  consists of two 1D convolution layers followed by a sigmoid function. For voxel-wise attention, we first compute the average of density embedding functions for all points within the voxel. Subsequently, the approach deployed for the point-wise feature is similarly applied, as follows:

$$\begin{aligned} \mathcal{D}_j^c &= \frac{1}{|L_j|} \sum_{p_i \in v_j} \mathcal{D}_i^c, \\ \hat{F}_j^v &= \text{Concat}(f_v(\mathcal{D}_j^c) \odot F_j^v, g(F_j^p)), \end{aligned} \quad (8)$$

where  $\mathcal{D}_j^c$  is a clipped density of voxel  $v_j$  and  $\hat{F}_j^v$  is a voxel-wise density discriminative feature and  $f_v$  consists of

---

**Algorithm 2** Enhanced-Mix3D Density Augmentation
 

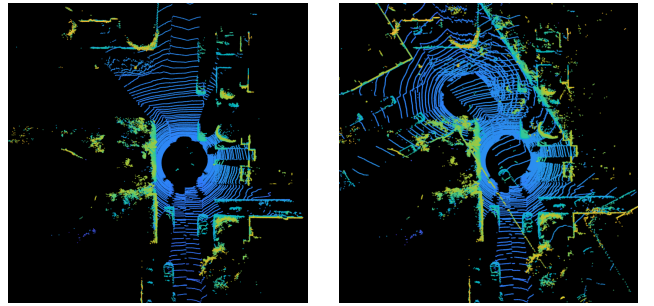
---

```

Input: Two point clouds  $\mathbf{P}_1 \in \mathbb{R}^{N \times 3}$  and  $\mathbf{P}_2 \in \mathbb{R}^{M \times 3}$ .
Output: Mixed point cloud  $\mathbf{P}_o \in \mathbb{R}^{(N+M) \times 3}$  and its corre-
   sponding density embedding  $\mathcal{D} \in \mathbb{R}^{(N+M) \times 4}$ 
1:  $\mathbf{R}_1 \leftarrow$  Z-axis-RandomRotation( $[-30^\circ, 30^\circ]$ )
2:  $\mathbf{R}_2 \leftarrow$  Z-axis-RandomRotation( $[-30^\circ, 30^\circ]$ )
3:  $\mathbf{t} \leftarrow$  X-axis-RandomTranslation( $[-25\text{m}, 25\text{m}]$ )
4:  $\tilde{\mathbf{P}}_2 \leftarrow \mathbf{R}_2(\mathbf{R}_1\mathbf{P}_2 + \mathbf{t})$   $\triangleright$  Transform point cloud
5:  $\mathbf{P}_o \leftarrow [\mathbf{P}_1; \tilde{\mathbf{P}}_2]$   $\triangleright$  Mix coordinates
6:  $\mathbf{O}_2 \leftarrow \mathbf{R}_2\mathbf{t}$   $\triangleright$  sensor center of  $\tilde{\mathbf{P}}_2$ 
7: for  $p_i \in \mathbf{P}_o$  do
8:    $\mathbf{d}_1 \leftarrow$  DensityOf( $p_i$ )  $\triangleright$  From Eq. 5
9:    $\mathbf{d}_2 \leftarrow$  DensityOf( $p_i - \mathbf{O}_2$ )  $\triangleright$  From Eq. 5
10:   $\mathcal{D}_i \leftarrow \sqrt{\mathbf{d}_1^2 + \mathbf{d}_2^2}$   $\triangleright$  Mix densities
11: end for

```

---



(a) Raw point cloud (b) Augmented point cloud

Fig. 4: Results of point cloud transformation through the proposed Density Augmentation on SemanticKITTI dataset.

two 1D convolution layers followed by a sigmoid function. An aggregation function  $g$  for the voxel-wise feature  $F_j^v$  is adjusted by voxel-wise attention and concatenated with the max pooled point-wise feature within the  $v_j$ . The extracted features pass through one 1D convolutional layer and are then used as input to the 3D backbone.

#### E. Density Augmentation

Our density alignment method operates on the premise that various datasets include canonical density domains. However, when datasets differ significantly in their density ranges, this assumption may falter. To address this potential shortcoming, we introduce a data augmentation method designed to expand the density spectrum. Among current 3D point cloud augmentation techniques, several methods [10], [13], [37] aim to address density variations, either directly or indirectly. For instance, Mix3D [37] increases density by combining two point clouds, while beam drop augmentation [10], [13] decreases it by skipping certain LiDAR channels. However, these techniques offer limited density variation ranges. Specifically, Mix3D, which merges two point clouds based on centroid alignment without additional translation, typically results in densities of only one or two times the original level, falling short in achieving a broader spectrum of beam-density levels.

To overcome these limitations, we propose Enhanced-Mix3D, an improved approach described in Alg. 2. Our

TABLE II: Comparison of domain generalization performance using the mIoU metric. All methods are based on MinkNet42 architecture. The bold and the underline indicate the best and the second-best performance, respectively.

Method	DA	Source	W	K	N	Source	K	W	N	Source	N	W	K
Base			75.37	49.40	47.83		57.31	35.24	37.42		<u>65.78</u>	38.65	36.24
IBN-Net [38]			<u>75.47</u>	51.13	44.72		57.74	36.99	38.74		65.31	36.53	36.93
MLDG [39]			72.47	48.94	48.64		56.26	35.39	36.77		61.32	36.33	32.70
COSMIX (W) [7]	✓	W	-	-	-	K	49.35	39.46	38.94	N	-	-	-
COSMIX (K) [7]	✓		66.68	44.71	<u>49.96</u>		-	-	-				
COSMIX (N) [7]	✓		65.68	40.99	47.98		49.98	38.05	43.25				
DGLSS [10]			75.28	<u>51.23</u>	49.61		<u>59.62</u>	40.67	44.83		65.32	<u>40.93</u>	38.98
Ours			<b>76.15</b>	<b>57.07</b>	<b>56.75</b>		<b>62.50</b>	<b>42.73</b>	<b>49.43</b>		<b>68.16</b>	<b>45.98</b>	<b>46.52</b>

TABLE III: Comparison of per-class performance (IoU) with DGLSS. All methods were trained using the MinkNet42 architecture on the SemanticKITTI dataset. The bold and the underline indicate the best and the second-best performance, respectively.

	Method	Car	Bicycle	Motor-cycle	Truck	Other vehicle	Pedestrian	Drivable surface	Side-walk	Walk-able	Vegetation	mIoU
K	Base	91.23	10.04	<u>35.69</u>	<u>52.89</u>	37.95	40.99	83.86	62.78	66.34	<b>91.33</b>	57.31
	DGLSS [10]	<b>92.76</b>	<u>11.99</u>	27.09	<b>72.50</b>	<b>45.95</b>	36.39	84.76	65.64	<u>67.98</u>	<u>91.28</u>	<u>59.62</u>
	Ours	<u>91.86</u>	<b>21.65</b>	<b>48.11</b>	26.84	<u>40.04</u>	<b>62.32</b>	<b>91.90</b>	<b>79.65</b>	<b>72.29</b>	90.31	<b>62.50</b>
N	Base	68.91	2.51	12.18	11.30	20.35	29.47	80.17	31.91	40.19	77.18	37.42
	DGLSS [10]	<b>76.36</b>	1.51	<b>35.18</b>	<u>26.47</u>	<u>25.49</u>	<u>37.09</u>	<u>82.03</u>	<u>38.12</u>	<u>44.20</u>	<u>81.79</u>	<u>44.83</u>
	Ours	<u>75.29</u>	<b>3.84</b>	<u>29.28</u>	<b>30.11</b>	<b>31.37</b>	<b>51.69</b>	<b>87.85</b>	<b>50.02</b>	<b>51.10</b>	<b>83.77</b>	<b>49.43</b>
W	Base	72.12	2.52	4.52	7.77	13.36	40.86	<u>64.92</u>	30.12	<b>34.84</b>	81.40	35.24
	DGLSS [10]	<u>82.26</u>	<b>4.85</b>	9.72	16.80	17.67	<u>52.55</u>	<b>68.20</b>	35.91	<u>33.33</u>	85.41	40.67
	Ours	<b>83.66</b>	<u>4.69</u>	<b>13.99</b>	<b>25.79</b>	<b>18.71</b>	<b>61.53</b>	63.19	<b>38.49</b>	28.66	<b>88.54</b>	<b>42.73</b>

method merges points and densities from two randomly selected point clouds with additional random translation. This Enhanced-Mix3D not only introduces a more continuous range of density variations but also ensures higher entropy and increased data diversity. Moreover, it accounts for the ego vehicle’s trajectory in determining new overlapping centers, as depicted in Fig. 4, leading to a more varied and flexible augmentation strategy. The process of density aggregation is followed by density clipping, similar to the process used for a single sweep. Beyond the aforementioned modification, we also enhance the density spectrum using a beam drop augmentation technique. Inspired by the works of [10], [13], we sample the vertical beams of the LiDAR at intervals of 2, effectively reducing the point cloud density by half. During training, both the Enhanced-Mix3D and beam drop augmentations are set with a probability of 0.5.

#### IV. EXPERIMENTS

In this section, we demonstrate the domain generalization performance of our method through extensive experiments. The implementation details and experimental settings of the proposed method are detailed in Sec. IV-A. The configuration of datasets used for evaluation is detailed in Sec. IV-B. A comparative analysis with recent domain generalization and domain adaptation methods is presented in Sec. IV-C. The effectiveness of individual components within the proposed DDFE is analyzed in Sec. IV-D.

##### A. Implementation Details

We employ the point head, inspired by Cylinder3D [1], to produce point-wise outputs as shown in Fig. 3. The process involves duplicating voxel-wise features from the 3D backbone and combining them with the corresponding point-wise

features  $\hat{F}^p$ . This amalgamation then undergoes processing through two MLP layers in the point head, culminating in the point-wise segmentation prediction. Simultaneously, the voxel head tackles voxel features with a sparse 3D convolution layer, employing a  $3 \times 3 \times 3$  kernel to create voxel-wise segmentation predictions in line with Cylinder3D’s methodology. For inference, we use only the point head that provides the point-by-point segmentation prediction.

For the loss functions in training, we incorporate the Lovasz-Softmax loss  $\mathcal{L}^{lovasz}$  [40] along with the Weighted Cross-Entropy loss  $\mathcal{L}^{wce}$ . The total loss is calculated by summing the voxel-wise and point-wise losses as follows:

$$\mathcal{L}_{total} = \mathcal{L}_{point}^{lovasz} + \mathcal{L}_{point}^{wce} + \mathcal{L}_{voxel}^{lovasz} + \mathcal{L}_{voxel}^{wce}, \quad (9)$$

where the weights are uniformly set to 1 for each of the four distinct loss functions. We use the Adam optimizer with an initial learning rate of  $1e-3$ . This rate is decreased by a factor of 0.99 with every epoch. The training is conducted over 30 epochs with a batch size of two on a single RTX 3090 GPU, and the epoch yielding the highest source validation mIoU was chosen. For voxelization, we adopt a cubic size of [20cm, 20cm, 20cm]. In cases where multiple point labels were found within a voxel, the voxel label is determined based on the predominant label, aligning with the approach in Cylinder3D [1].

The total inference time of our method for processing a single frame with the nuScenes dataset on the NVIDIA RTX 3090 is 44ms. It’s important to note that integrating our DDFE module into the MinkNet42 architecture contributes an additional 8ms to the computation time, with the MinkNet42 architecture requiring 36ms. This integration also slightly increases the model complexity, adding about 23.8k parameters (+0.06%). Furthermore, implementing density augmentation

TABLE IV: Comparison of per-class performance (IoU) with DA/DG methods. All methods are based on MinkNet42 architecture. The symbol † denotes methods necessitating ego-motion knowledge. The bold and the underline indicate the best and the second-best performance, respectively.

	Method	DA	Car	Bicycle	Motor-cycle	Truck	Other vehicle	Pedestrian	Drivable surface	Sidewalk	Terrain	Vegetation	mIoU
$K \rightarrow N$	Base		50.7	<u>5.7</u>	6.0	21.7	24.8	29.2	<b>89.1</b>	42.0	23.1	85.8	37.8
	FADA [41]	✓	69.1	1.9	21.4	42.9	20.5	12.6	84.3	43.6	38.3	80.0	41.5
	CLAN [42]	✓	73.1	1.7	16.3	31.4	19.1	13.5	85.7	45.7	<u>50.1</u>	81.4	41.8
	DAST [43]	✓	73.2	2.1	24.4	<u>44.6</u>	22.4	18.2	77.6	39.5	43.2	81.2	42.6
	DCFNet [8]	✓	74.9	1.8	28.9	<u>33.9</u>	21.6	19.9	84.5	44.6	46.3	83.6	44.0
	CutMix [44]		75.5	0.1	14.0	26.6	22.6	3.9	86.6	36.5	19.7	85.6	37.1
	Copy-Paste [45]		<u>77.9</u>	3.1	11.1	21.7	<u>31.2</u>	7.8	88.0	38.8	19.6	<u>86.2</u>	38.5
	Mix3D [37]		72.1	0.0	34.8	11.7	26.4	28.5	83.3	41.0	46.4	<b>86.5</b>	43.1
	PolarMix [46]		74.1	1.7	<u>41.9</u>	26.9	23.8	<u>30.5</u>	85.1	42.7	45.3	<u>86.2</u>	45.8
	LiDomAug† [12]		<b>79.2</b>	<b>5.8</b>	28.0	<b>49.3</b>	<b>32.1</b>	13.8	88.0	42.0	35.4	85.1	<u>45.9</u>
Ours		76.0	<u>5.7</u>	<b>42.3</b>	33.9	26.7	<b>49.5</b>	88.5	<b>49.8</b>	<b>50.2</b>	78.2	<b>50.1</b>	
$N \rightarrow K$	Base		78.5	0.0	8.2	3.4	11.1	34.5	66.3	35.8	39.4	84.2	36.1
	FADA [41]	✓	83.3	<u>39.0</u>	24.5	8.7	3.6	33.6	72.7	39.4	36.0	82.1	42.3
	CLAN [42]	✓	86.0	21.4	9.2	13.5	5.7	<u>42.8</u>	77.8	<b>51.0</b>	47.6	84.6	43.9
	DAST [43]	✓	90.8	<b>40.8</b>	24.0	11.5	5.2	41.7	76.7	45.3	48.5	84.5	46.9
	DCFNet [8]	✓	91.7	34.3	24.5	18.5	11.6	<b>49.1</b>	78.6	47.5	49.8	86.4	<b>49.2</b>
	CutMix [44]		81.2	0.0	5.3	9.1	<b>17.4</b>	11.8	73.6	45.5	46.8	85.7	37.6
	Copy-Paste [45]		85.7	0.0	8.2	12.8	6.5	28.6	80.8	47.4	53.8	87.2	41.1
	Mix3D [37]		<b>93.1</b>	10.4	<u>31.3</u>	17.0	<u>14.1</u>	34.2	71.8	40.7	44.6	<b>89.5</b>	44.7
	PolarMix [46]		75.9	19.4	19.7	9.6	3.0	18.3	75.0	43.1	48.9	77.8	39.1
	LiDomAug† [12]		<u>92.6</u>	31.6	<b>42.5</b>	<u>21.6</u>	6.4	34.4	70.0	47.1	<b>59.4</b>	77.5	<u>48.3</u>
Ours		89.5	4.7	29.5	<b>22.4</b>	6.3	33.7	<b>81.9</b>	<u>50.7</u>	<u>56.5</u>	<u>88.2</u>	46.3	

during training on the nuScenes dataset requires an additional 60ms per scan.

## B. Datasets

In our experimental setup, we employ three datasets: Waymo [4], SemanticKITTI [5], and nuScenes [6]. Notably, the Waymo and SemanticKITTI datasets use 64-channel LiDAR, while the nuScenes employs a 32-channel LiDAR. For detailed information, please refer to Fig. 2 and Tab. I. In line with methods from previous studies [10], [12], we split the nuScenes sequences into 700 for training and 150 for validation. The Waymo dataset is partitioned into 798 sequences for training and 202 for validation. Regarding the SemanticKITTI dataset, we use sequences 00 to 10 for training, setting aside sequence 08 exclusively for validation.

To support domain generalization experiments, we standardize the coordinate system across all datasets, aligning it with LiDAR’s coordinate framework. In this unified system, the forward direction of the ego vehicle aligns with the x-axis, the leftward direction with the y-axis, and the upward direction with the z-axis. We also remove the ego vehicle’s point cloud data in the preprocessing phase to enhance computational efficiency. For the LiDAR in the Waymo dataset, it’s noteworthy that the vertical beam inclinations are not uniformly distributed. Detailed information about each vertical beam angle is provided within the dataset itself [4].

## C. Comparison to State-of-the-Art DA/DG Methods

The domain of LiDAR-based semantic segmentation generalization is still developing, and standardized experimental protocols are not yet established. Consequently, different methods have employed varied experimental approaches. To ensure equitable comparisons, we adopt the experimental

settings used in leading studies such as LiDomAug [12] and DGLSS [10]. In this setup, we compare our method with various Domain Adaptation (DA) techniques. Moreover, we demonstrate the efficacy of our approach by conducting comparisons within the framework of Rangeview-based DA methods, as detailed in [29].

1) *Experiments in the DGLSS Setting:* We compare our proposed method with a domain adaptation method COSMIX [7], and domain generalization methods IBN-Net [38], MLDG [39] and DGLSS [10] in the domain generalization experimental setting as introduced in DGLSS [10]. We utilize the Waymo [4], SemanticKITTI [5], and nuScenes [6] datasets. For consistency, we choose MinkowskiNet [24] for our backbone network same as DGLSS.

Results in Tab. II indicate that the proposed method consistently outperforms DGLSS across all datasets, including the Waymo, SemanticKITTI, and nuScenes datasets. Impressively, our method not only demonstrates superior domain generalization performance but also dominates in the source-to-source settings ( $W \rightarrow W$ ,  $K \rightarrow K$ ,  $N \rightarrow N$ ). While DGLSS customizes its augmentation ratios for each dataset, our approach achieves better domain generalization performance using a consistent hyperparameter configuration across all datasets. Our method achieves an average increase of 12.9% over DGLSS for unseen datasets using Waymo as the source data ( $W \rightarrow K$ ,  $W \rightarrow N$ ). When SemanticKITTI is the source data, we observe an average improvement of 7.8% for other unseen datasets ( $K \rightarrow W$ ,  $K \rightarrow N$ ). Lastly, utilizing nuScenes as the source data results in our approach surpassing DGLSS by an average of 15.8% on other unseen datasets ( $N \rightarrow W$ ,  $N \rightarrow K$ ). Tab. III represents the class-specific IoU results using SemanticKITTI as the source dataset. In this context, our method outperforms others in 8 out of 10 classes for the ( $K \rightarrow N$ ) scenario and in 7 out of 10 classes for the ( $K \rightarrow W$ ) scenario. These results

TABLE V: Comparison of per-class performance (IoU) with DA/DG methods. All methods are based on C&L architecture. The symbol † denotes methods necessitating ego-motion knowledge. The bold and the underline indicate the best and the second-best performance, respectively.

	Method	DA	Car	Bicycle	Motor-cycle	Truck	Other vehicle	Pedestrian	Drivable surface	Sidewalk	Terrain	Vegetation	mIoU
$N \rightarrow N$	Base		<u>55.3</u>	0.1	3.4	<u>2.5</u>	4.5	4.7	79.2	32.2	21.7	74.0	27.8
	SWD [47]	✓	-	-	-	-	-	-	-	-	-	-	27.7
	3DGCA [25]	✓	-	-	-	-	-	-	-	-	-	-	27.4
	C&L† [11]	✓	-	-	-	-	-	-	-	-	-	-	31.6
	LiDAR-UDA† [30]	✓	<b>73.5</b>	<u>0.9</u>	<u>15.9</u>	0.9	<u>25.7</u>	<b>40.8</b>	<b>87.4</b>	<u>42.3</u>	<u>47.9</u>	<b>83.2</b>	41.8
	LiDomAug† [12]		-	-	-	-	-	-	-	-	-	-	-
Ours		<b>73.5</b>	<b>1.7</b>	<b>35.9</b>	<b>34.2</b>	<b>27.4</b>	<b>40.3</b>	<b>85.1</b>	<b>45.4</b>	<b>48.5</b>	<b>78.9</b>	<b>47.1</b>	
$K \rightarrow K$	Base		58.0	<u>0.5</u>	4.4	3.8	<u>5.0</u>	12.6	33.8	2.8	30.1	80.9	23.2
	SWD [47]	✓	-	-	-	-	-	-	-	-	-	-	24.5
	3DGCA [25]	✓	-	-	-	-	-	-	-	-	-	-	23.9
	C&L† [11]	✓	-	-	-	-	-	-	-	-	-	-	33.7
	LiDAR-UDA† [30]	✓	<b>86.2</b>	0.0	13.9	<u>9.3</u>	3.2	16.5	65.7	6.1	<u>54.1</u>	<u>85.7</u>	34.0
	LiDomAug† [12]		83.7	0.0	<u>16.6</u>	5.4	<b>13.4</b>	<b>29.6</b>	<u>67.4</u>	<u>25.4</u>	<b>56.5</b>	81.2	<u>37.9</u>
Ours		<u>84.6</u>	<b>8.7</b>	<b>27.6</b>	<b>15.8</b>	2.6	<u>27.6</u>	<b>75.6</b>	<b>27.6</b>	46.8	<b>86.1</b>	<b>40.3</b>	

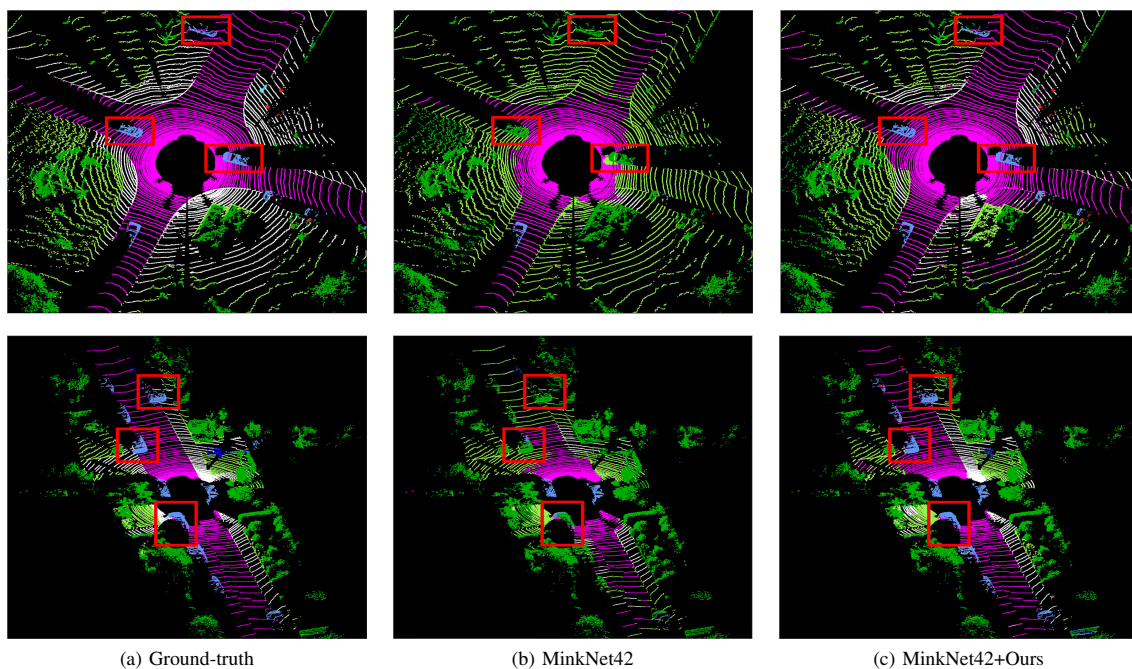


Fig. 5: Qualitative comparison with MinkNet42 backbone. ( $N \rightarrow K$ )

demonstrate the effectiveness of our method.

2) *Experiments in the LiDomAug Setting:* We benchmark the proposed method against various augmentation methods, including CutMix [44], Copy-Paste [45], Mix3D [37], PolarMix [46], and domain adaptation methods like SWD [47], 3DGCA [25], Complete & Label [11], LiDAR-UDA [30], CLAN [42], FADA [41], DAST [43] and DCFNet [8]. We employ the experimental setting proposed by LiDomAug [12], using SemanticKITTI [5] and nuScenes [6] datasets. We conduct two distinct experiments: one using the MinkowskiNet [24] as the backbone network and the other using the Complete and Label (C&L) [11].

Tab. IV shows the performance of various data augmentation methods, domain adaptation methods, and our proposed method, all using MinkNet42 as the backbone. The results for CLAN [42], FADA [41], DAST [43], and DCFNet [8] are taken from the DCFNet publication. While our method shows

slightly lower performance than LiDomAug in the ( $N \rightarrow K$ ) scenario, it excels in the ( $K \rightarrow N$ ) scenario, surpassing all other augmentation methods. Our method demonstrates a significant 9.2% improvement in performance over LiDomAug, which relies on ego-motion and multi-frame information, highlighting its robustness and effectiveness. Moreover, although our approach falls short by 5.9% compared to the latest DA technique, DCFNet [8], in the ( $N \rightarrow K$ ) scenario, it excels in the ( $K \rightarrow N$ ) scenario, outperforming DCFNet by 13.9%. The qualitative results, as shown in Fig. 5 and Fig. 6, underscore the significant enhancement in domain generalization performance of the 3D backbone network by our method.

In experiments using C&L [11] as the backbone (see Tab. V), our method notably increases mIoU by 49.1%, 12.7%, and 20.2% in the ( $K \rightarrow N$ ) scenario compared to C&L [11], LiDAR-UDA [30], and LiDomAug [12], respectively. In the transition from the 32-channel sparse dataset



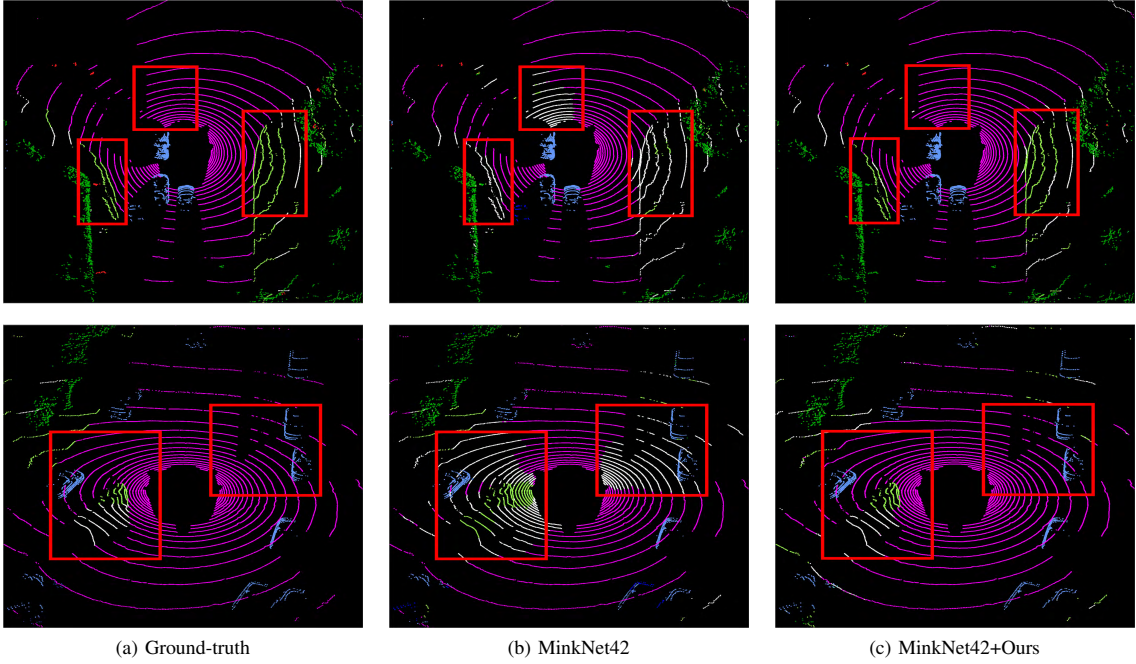


Fig. 6: Qualitative comparison with MinkNet42 backbone. ( $K \rightarrow N$ )

TABLE VI: Comparison of per-class performance (IoU) with rangeview-based DA methods. The bold and the underline indicate the best and the second-best performance, respectively.

	Backbone	Method	Car	Bicycle	Motor-cycle	Other vehicle	Pedestrian	Truck	Drivable surface	Sidewalk	Terrain	Vegetation	Man-made	mIoU	
$K \rightarrow N$	SalsaNext (Rangeview)	Base	35.7	0.2	0.4	5.7	7.5	8.1	73.8	15.0	14.9	8.3	51.4	20.1	
		CORAL [48]	51.0	0.9	6.0	4.0	25.9	<b>29.9</b>	82.6	27.1	27.0	55.3	56.7	33.3	
		MEnt [49]	57.4	2.2	4.6	6.4	22.6	19.3	82.3	28.8	29.9	46.8	64.2	33.1	
		AEnt [49]	57.4	1.1	8.6	6.7	24.0	10.1	81.0	25.4	26.6	34.2	58.9	30.4	
		(M+A)Ent [49]	57.3	1.1	2.3	6.8	23.4	7.9	<u>83.5</u>	32.6	31.8	43.3	62.3	32.0	
		SWD [47]	45.3	2.1	2.2	3.4	25.9	10.6	80.7	26.5	30.1	43.9	60.2	30.1	
		Rochan <i>et al.</i> [29]	54.4	<u>3.0</u>	1.9	7.6	<u>27.7</u>	15.8	82.2	29.6	<u>34.0</u>	57.9	65.7	34.5	
		MinkNet42 (Voxel)	Base	69.7	<b>5.3</b>	<u>26.2</u>	<b>18.3</b>	26.5	17.5	82.2	<u>35.6</u>	30.6	<u>65.2</u>	69.7	<u>40.6</u>
		Ours	<b>75.3</b>	1.6	<b>44.9</b>	<u>15.7</u>	<b>28.5</b>	<u>19.4</u>	<b>87.8</b>	<b>48.0</b>	<b>44.4</b>	<b>67.3</b>	<b>72.1</b>	<b>45.9</b>	
		$N \rightarrow K$	SalsaNext (Rangeview)	Base	7.7	0.1	0.9	0.6	6.4	0.4	30.4	5.7	28.4	27.8	30.2
CORAL [48]	47.3			10.4	6.9	<u>5.1</u>	10.8	0.7	24.8	13.8	31.7	58.8	45.5	23.2	
MEnt [49]	27.1			2.0	2.3	3.4	9.5	0.4	29.3	11.3	28.0	35.8	39.0	17.1	
AEnt [49]	42.4			4.5	6.9	2.8	6.7	0.7	16.1	7.0	26.1	46.1	42.0	18.3	
(M+A)Ent [49]	49.6			5.9	4.3	<b>6.4</b>	9.6	2.6	22.5	12.7	30.3	57.4	49.1	22.8	
SWD [47]	34.2			2.7	1.5	2.0	5.3	0.9	28.8	20.5	28.3	38.2	36.7	18.1	
Rochan <i>et al.</i> [29]	49.6			4.6	6.3	2.0	12.5	1.8	<u>25.2</u>	<u>25.2</u>	<u>42.3</u>	43.4	45.3	23.5	
MinkNet42 (Voxel)	Base			58.7	<u>11.3</u>	<u>12.6</u>	2.1	<b>24.2</b>	<u>11.6</u>	63.3	14.7	22.1	64.5	64.9	<u>31.8</u>
Ours	<b>87.1</b>			<b>15.0</b>	<b>20.1</b>	4.1	<u>20.4</u>	<b>16.9</b>	<b>83.6</b>	<b>45.9</b>	<b>54.7</b>	<b>81.7</b>	<b>76.8</b>	<b>46.0</b>	

( $N \rightarrow K$ ), our approach shows a 19.6% improvement in mIoU over C&L and a 6.3% advantage over LiDomAug. C&L and LiDomAug have an inherent advantage in handling sparse datasets. This advantage is due to their strategy of using multi-frame point clouds combined with known ego-motion to transform sparse data into denser formats. As a result, the difference in performance between these methods and ours is less marked in the ( $N \rightarrow K$ ) scenario compared to the ( $K \rightarrow N$ ) context.

3) *Comparison with Rangeview-based DA Methods:* To further validate the effectiveness of our method, we perform comparative experiments between our method and various rangeview-based Domain Adaptation (DA) techniques [47]–[49], using the 11-class setting from [29]. While these DA methods employ SalsaNext [15], a rangeview-based model, as their baseline, our experiments are based on a 3D voxel-based network, MinkNet42 [24]. The comparative results,

except for the MinkNet42 base and our method, are sourced from [29]. Interestingly, even without our proposed method, the MinkNet42 model demonstrates superior generalization performance compared to the rangeview-based backbones with domain adaptation techniques [29], [47]–[49]. With the application of our method, MinkNet42’s performance increases by 13.1% in the ( $K \rightarrow N$ ) scenario and by 44.7% in the ( $N \rightarrow K$ ) scenario, relative to its baseline.

Rangeview images, trained on uniformly dense 2D projections, often face challenges in domain generalization across different densities. In contrast, 3D voxel-based methods, trained across varying densities in 3D space, are better equipped for adaptation to domain changes. When compared to [29], our method shows significantly higher performance improvements of 33.0% and 95.7% in respective scenarios. The limited performance of the method [29] is likely due to information loss during the rangeview upsampling process,

TABLE VII: Ablation study on feature embedding components (mIoU). (a) Point-voxel encoding. (b) Density-aware embedding module. (c) Density clipping. (d) Density-Augmentation.

(a)	(b)	(c)	(d)	K→N	N→K
				40.7	31.4
✓				43.0 (+5.7%)	35.0 (+11.5%)
✓	✓			45.7 (+12.3%)	40.5 (+29.0%)
✓	✓	✓		46.2 (+13.5%)	41.8 (+33.1%)
✓	✓	✓	✓	<b>50.1 (+23.1%)</b>	<b>46.3 (+47.5%)</b>

despite their efforts to align projection points between training and target datasets.

#### D. Ablation Studies

To validate the contributions of each component in our method, we conduct ablation studies focusing on point-voxel encoding, the density-aware embedding module, density soft clipping, and density augmentation. These experiments align with the LiDomAug [12] settings.

1) *Density discriminative feature embedding*: In Tab. VII, which extends Tab. IV, we present an ablation study using the experimental setup proposed by LiDomAug [12] and based on MinkowskiNet42. This study highlights the key components of our DDFE module: (a) point-voxel encoding, (b) density-aware embedding module, and (c) density clipping. Additionally, we evaluate (d) the effect of our density augmentation method. When all these components are utilized, we observe a notable performance increase of +13.5% in the (K→N) scenario and +33.1% in the (N→K) scenario, compared to the baseline. The density-aware embedding module emerges as a particularly impactful factor, closely followed by the point-voxel feature encoding, which underscores its significance. The density soft clipping method proves its worth by enhancing the model’s adaptability to new density patterns, while the improvements due to the density clipping technique underscore the challenges models face with unfamiliar density distributions.

2) *Data augmentation*: In Tab. VIII, we compare our density augmentation method with existing data augmentation techniques. To adapt the Mix3D method to our DDFE module, we modify the density value mixing process as outlined in Alg. 2, specifically at line #10. Our analysis reveals that aligning the training dataset with the target density characteristics is crucial for performance improvement. This is evident with Beam drop augmentation in the density decreasing (K→N) scenarios and Mix3D in density increasing (N→K) scenarios, where each method leads to substantial gains. Conversely, scenarios where this alignment is not achieved see limited performance improvements. Furthermore, our Enhanced-Mix3D (E-Mix3D) outperforms the original Mix3D during the transition from nuScenes to KITTI, benefiting from a more varied density distribution. Our approach, which combines E-Mix3D with beam drop augmentation, not only surpasses methods without augmentation, showing significant performance improvements of +8.4% and +10.8%, but also yields additional gains of +1.8% and +4.0% over the standard Mix3D and beam drop combination. This highlights the effectiveness of our density augmentation strategy in enhancing performance across different scenarios.

TABLE VIII: Ablation study on data augmentation methods using MinkNet42 with DDFE (mIoU).

Method	K→N	N→K
w/o aug	46.2	41.8
Beam drop [13]	49.1 (+6.3%)	42.7 (+2.2%)
Mix3D [37]	46.7 (+1.1%)	44.0 (+5.3%)
Mix3D + Beam drop	49.2 (+6.5%)	44.5 (+6.5%)
E-Mix3D	48.7 (+5.4%)	45.4 (+8.6%)
E-Mix3D + Beam drop	<b>50.1 (+8.4%)</b>	<b>46.3 (+10.8%)</b>

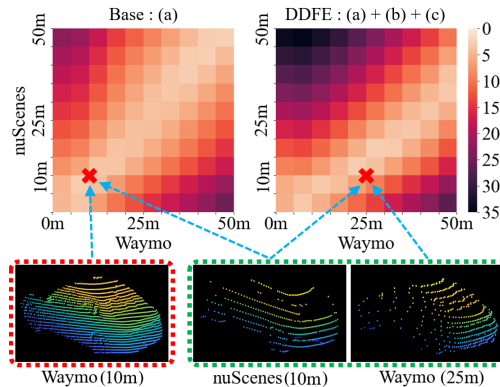


Fig. 7: Visualization of feature similarities between the Waymo (64-channel) and the nuScenes (32-channel) datasets. (a) A point-voxel feature encoding method. (b) A density-aware embedding module. (c) A density soft clipping. Our DDFE combines all modules (a), (b), and (c).

3) *Feature similarity*: To analyze the effects of DDFE, we investigate the feature similarity between the source and unseen dataset as shown in Fig. 7. For our analysis, we consider the input voxel features  $F^v$  of the 3D backbone model generated by the DDFE module. We begin our investigation with a baseline model that employs a point-voxel feature encoding method. This is then compared against our method integrated a density-aware embedding module and a density soft clipping. Both of these models are trained on the nuScenes dataset and then tested on the Waymo dataset, which served as the unseen dataset. We compute similarity values based on the L2 distance between the average features over specified distance intervals (e.g., 0-5m, ..., 45-50m) of each dataset. From the visualization in Fig. 7, the baseline model consistently demonstrates higher feature similarity at similar distances, regardless of density. This can be attributed to the feature encoding process that directly embeds the 3D coordinates of points. On the other hand, the model that combines the baseline with the density-aware embedding module with soft clipping shows pronounced feature similarity within consistent density distributions, even when making comparisons between the source and unseen datasets.

## V. CONCLUSION

In this paper, we introduce a new perspective for domain generalization, utilizing the inherent property of LiDAR where density varies with distance. Based on this perspective, we propose a density discriminative feature embedding module called DDFE, which enhances the ability to discern densities by

estimating expected densities from LiDAR beams. As a result, it improves the generalization performance, especially when transitioning between the source dataset and previously unseen datasets. In addition to the core methodology, we also present a simple and effective data augmentation technique. This method amplifies the density spectrum of a point cloud without relying on ego-motion or sequential labeled data. Extensive experiments on the SemanticKITTI, Waymo, and nuScenes datasets demonstrate the effectiveness of the proposed method in elevating the domain generalization performance of LiDAR semantic segmentation. In future work, we aim to extend domain generalization for other LiDAR-based perception tasks such as 3D object detection by leveraging object-wise density discriminative features in conjunction with point-wise density embedding.

## REFERENCES

- [1] X. Zhu, H. Zhou, T. Wang, F. Hong, Y. Ma, W. Li, H. Li, and D. Lin, "Cylindrical and asymmetrical 3d convolution networks for lidar segmentation," in *Proceedings of IEEE Conference on Computer Vision and Pattern Recognition (CVPR)*, 2021, pp. 9939–9948.
- [2] Y. Hou, X. Zhu, Y. Ma, C. C. Loy, and Y. Li, "Point-to-voxel knowledge distillation for lidar semantic segmentation," in *Proceedings of IEEE Conference on Computer Vision and Pattern Recognition (CVPR)*, 2022, pp. 8479–8488.
- [3] A. Ando, S. Gidaris, A. Bursuc, G. Puy, A. Boulch, and R. Marlet, "Rangevit: Towards vision transformers for 3d semantic segmentation in autonomous driving," in *Proceedings of IEEE Conference on Computer Vision and Pattern Recognition (CVPR)*, 2023, pp. 5240–5250.
- [4] P. Sun *et al.*, "Scalability in perception for autonomous driving: Waymo open dataset," in *Proceedings of IEEE Conference on Computer Vision and Pattern Recognition (CVPR)*, 2020, pp. 2446–2454.
- [5] J. Behley, M. Garbade, A. Milioto, J. Quenzel, S. Behnke, C. Stachniss, and J. Gall, "Semantickitti: A dataset for semantic scene understanding of lidar sequences," in *Proceedings of IEEE International Conference on Computer Vision (ICCV)*, 2019, pp. 9297–9307.
- [6] H. Caesar *et al.*, "nuscenes: A multimodal dataset for autonomous driving," in *Proceedings of IEEE Conference on Computer Vision and Pattern Recognition (CVPR)*, 2020, pp. 11 621–11 631.
- [7] C. Saltori, F. Galasso, G. Fiameni, N. Sebe, E. Ricci, and F. Poiesi, "Cosmix: Compositional semantic mix for domain adaptation in 3d lidar segmentation," in *Proceedings of European Conference on Computer Vision (ECCV)*. Springer, 2022, pp. 586–602.
- [8] Z. Yuan, C. Wen, M. Cheng, Y. Su, W. Liu, S. Yu, and C. Wang, "Category-level adversaries for outdoor lidar point clouds cross-domain semantic segmentation," *IEEE Transactions on Intelligent Transportation Systems*, vol. 24, no. 2, pp. 1982–1993, 2022.
- [9] L. Kong, N. Quader, and V. E. Liang, "Conda: Unsupervised domain adaptation for lidar segmentation via regularized domain concatenation," in *Proceedings of IEEE International Conference on Robotics and Automation (ICRA)*. IEEE, 2023, pp. 9338–9345.
- [10] H. Kim, Y. Kang, C. Oh, and K.-J. Yoon, "Single domain generalization for lidar semantic segmentation," in *Proceedings of IEEE Conference on Computer Vision and Pattern Recognition (CVPR)*, 2023, pp. 17 587–17 598.
- [11] L. Yi, B. Gong, and T. Funkhouser, "Complete & label: A domain adaptation approach to semantic segmentation of lidar point clouds," in *Proceedings of IEEE Conference on Computer Vision and Pattern Recognition (CVPR)*, 2021, pp. 15 363–15 373.
- [12] K. Ryu, S. Hwang, and J. Park, "Instant domain augmentation for lidar semantic segmentation," in *Proceedings of IEEE Conference on Computer Vision and Pattern Recognition (CVPR)*, 2023, pp. 9350–9360.
- [13] Y. Wei, Z. Wei, Y. Rao, J. Li, J. Zhou, and J. Lu, "Lidar distillation: Bridging the beam-induced domain gap for 3d object detection," in *Proceedings of European Conference on Computer Vision (ECCV)*. Springer, 2022, pp. 179–195.
- [14] Q. Hu, D. Liu, and W. Hu, "Density-insensitive unsupervised domain adaptation on 3d object detection," in *Proceedings of the IEEE/CVF Conference on Computer Vision and Pattern Recognition*, 2023, pp. 17 556–17 566.
- [15] T. Cortinhal, G. Tzelepis, and E. Erdal Aksoy, "Salsanext: Fast, uncertainty-aware semantic segmentation of lidar point clouds," in *Advances in Visual Computing: 15th International Symposium, ISVC 2020, San Diego, CA, USA, October 5–7, 2020, Proceedings, Part II 15*. Springer, 2020, pp. 207–222.
- [16] Y. Zhang, Z. Zhou, P. David, X. Yue, Z. Xi, B. Gong, and H. Foroosh, "Polarnet: An improved grid representation for online lidar point clouds semantic segmentation," in *Proceedings of IEEE Conference on Computer Vision and Pattern Recognition (CVPR)*, 2020, pp. 9601–9610.
- [17] K. Peng, J. Fei, K. Yang, A. Roitberg, J. Zhang, F. Bieder, P. Heidenreich, C. Stillner, and R. Stiefelhagen, "Mass: Multi-attentional semantic segmentation of lidar data for dense top-view understanding," *IEEE Transactions on Intelligent Transportation Systems*, vol. 23, no. 9, pp. 15 824–15 840, 2022.
- [18] T.-H. Chen and T. S. Chang, "Rangeseg: Range-aware real time segmentation of 3d lidar point clouds," *IEEE Transactions on Intelligent Vehicles*, vol. 7, no. 1, pp. 93–101, 2022.
- [19] H.-X. Cheng, X.-F. Han, and G.-Q. Xiao, "Transrvnet: Lidar semantic segmentation with transformer," *IEEE Transactions on Intelligent Transportation Systems*, vol. 24, no. 6, pp. 5895–5907, 2023.
- [20] H. Thomas, C. R. Qi, J.-E. Deschaud, B. Marcotegui, F. Goulette, and L. J. Guibas, "Kpconv: Flexible and deformable convolution for point clouds," in *Proceedings of IEEE International Conference on Computer Vision (ICCV)*, 2019, pp. 6411–6420.
- [21] Q. Hu, B. Yang, L. Xie, S. Rosa, Y. Guo, Z. Wang, N. Trigoni, and A. Markham, "Randla-net: Efficient semantic segmentation of large-scale point clouds," in *Proceedings of IEEE Conference on Computer Vision and Pattern Recognition (CVPR)*, 2020, pp. 11 108–11 117.
- [22] S. Fan, Q. Dong, F. Zhu, Y. Lv, P. Ye, and F.-Y. Wang, "Scf-net: Learning spatial contextual features for large-scale point cloud segmentation," in *Proceedings of IEEE Conference on Computer Vision and Pattern Recognition (CVPR)*, 2021, pp. 14 504–14 513.
- [23] B. Graham, M. Engelcke, and L. Van Der Maaten, "3d semantic segmentation with submanifold sparse convolutional networks," in *Proceedings of the IEEE conference on computer vision and pattern recognition*, 2018, pp. 9224–9232.
- [24] C. Choy, J. Gwak, and S. Savarese, "4d spatio-temporal convnets: Minkowski convolutional neural networks," in *Proceedings of IEEE Conference on Computer Vision and Pattern Recognition (CVPR)*, 2019, pp. 3075–3084.
- [25] B. Wu, X. Zhou, S. Zhao, X. Yue, and K. Keutzer, "Squeezesegv2: Improved model structure and unsupervised domain adaptation for road-object segmentation from a lidar point cloud," in *Proceedings of IEEE International Conference on Robotics and Automation (ICRA)*, 2019, pp. 4376–4382.
- [26] J. Yang, S. Shi, Z. Wang, H. Li, and X. Qi, "St3d: Self-training for unsupervised domain adaptation on 3d object detection," in *Proceedings of IEEE Conference on Computer Vision and Pattern Recognition (CVPR)*, 2021, pp. 10 368–10 378.
- [27] X. Peng, X. Zhu, and Y. Ma, "Cl3d: Unsupervised domain adaptation for cross-lidar 3d detection," in *Proceedings of the AAAI Conference on Artificial Intelligence (AAAI)*, vol. 37, no. 2, 2023, pp. 2047–2055.
- [28] C. Saltori, S. Lathuilière, N. Sebe, E. Ricci, and F. Galasso, "Sf-uda 3d: Source-free unsupervised domain adaptation for lidar-based 3d object detection," in *Proceedings of International Conference on 3D Vision (3DV)*, 2020, pp. 771–780.
- [29] M. Rochan, S. Aich, E. R. Corral-Soto, A. Nabatchian, and B. Liu, "Unsupervised domain adaptation in lidar semantic segmentation with self-supervision and gated adapters," in *Proceedings of IEEE International Conference on Robotics and Automation (ICRA)*, 2022, pp. 2649–2655.
- [30] A. Shaban, J. Lee, S. Jung, X. Meng, and B. Boots, "Lidar-uda: Self-ensembling through time for unsupervised lidar domain adaptation," in *Proceedings of IEEE International Conference on Computer Vision (ICCV)*, 2023, pp. 19 784–19 794.
- [31] A. Lehner, S. Gasperini, A. Marcos-Ramiro, M. Schmidt, M.-A. N. Mahani, N. Navab, B. Busam, and F. Tombari, "3d-vfield: Adversarial augmentation of point clouds for domain generalization in 3d object detection," in *Proceedings of IEEE Conference on Computer Vision and Pattern Recognition (CVPR)*, 2022, pp. 17 295–17 304.
- [32] A. Xiao, J. Huang, W. Xuan, R. Ren, K. Liu, D. Guan, A. El Saddik, S. Lu, and E. P. Xing, "3d semantic segmentation in the wild: Learning generalized models for adverse-condition point clouds," in *Proceedings of IEEE Conference on Computer Vision and Pattern Recognition (CVPR)*, 2023, pp. 9382–9392.
- [33] J. Sanchez, J.-E. Deschaud, and F. Goulette, "Domain generalization of 3d semantic segmentation in autonomous driving," in *Proceedings of*

*IEEE International Conference on Computer Vision (ICCV)*, 2023, pp. 18 077–18 087.

- [34] M. Li, Y. Zhang, X. Ma, Y. Qu, and Y. Fu, “Bev-dg: Cross-modal learning under bird’s-eye view for domain generalization of 3d semantic segmentation,” in *Proceedings of IEEE International Conference on Computer Vision (ICCV)*, 2023, pp. 11 632–11 642.
- [35] C. Saltori, A. Osep, E. Ricci, and L. Leal-Taixé, “Walking your lidog: A journey through multiple domains for lidar semantic segmentation,” in *Proceedings of IEEE International Conference on Computer Vision (ICCV)*, 2023, pp. 196–206.
- [36] C. R. Qi, H. Su, K. Mo, and L. J. Guibas, “Pointnet: Deep learning on point sets for 3d classification and segmentation,” in *Proceedings of IEEE Conference on Computer Vision and Pattern Recognition (CVPR)*, 2017, pp. 652–660.
- [37] A. Nekrasov, J. Schult, O. Litany, B. Leibe, and F. Engelmann, “Mix3d: Out-of-context data augmentation for 3d scenes,” in *Proceedings of International Conference on 3D Vision (3DV)*, 2021, pp. 116–125.
- [38] X. Pan, P. Luo, J. Shi, and X. Tang, “Two at once: Enhancing learning and generalization capacities via ibn-net,” in *Proceedings of European Conference on Computer Vision (ECCV)*, 2018, pp. 464–479.
- [39] D. Li, Y. Yang, Y.-Z. Song, and T. Hospedales, “Learning to generalize: Meta-learning for domain generalization,” in *Proceedings of the AAAI Conference on Artificial Intelligence (AAAI)*, vol. 32, no. 1, 2018.
- [40] M. Berman, A. R. Triki, and M. B. Blaschko, “The lovasz-softmax loss: A tractable surrogate for the optimization of the intersection-over-union measure in neural networks,” in *Proceedings of IEEE Conference on Computer Vision and Pattern Recognition (CVPR)*, 2018, pp. 4413–4421.
- [41] H. Wang, T. Shen, W. Zhang, L.-Y. Duan, and T. Mei, “Classes matter: A fine-grained adversarial approach to cross-domain semantic segmentation,” in *Proceedings of European Conference on Computer Vision (ECCV)*. Springer, 2020, pp. 642–659.
- [42] Y. Luo, L. Zheng, T. Guan, J. Yu, and Y. Yang, “Taking a closer look at domain shift: Category-level adversaries for semantics consistent domain adaptation,” in *Proceedings of IEEE Conference on Computer Vision and Pattern Recognition (CVPR)*, 2019, pp. 2507–2516.
- [43] F. Yu, M. Zhang, H. Dong, S. Hu, B. Dong, and L. Zhang, “Dast: Unsupervised domain adaptation in semantic segmentation based on discriminator attention and self-training,” in *Proceedings of the AAAI Conference on Artificial Intelligence (AAAI)*, vol. 35, no. 12, 2021, pp. 10 754–10 762.
- [44] S. Yun, D. Han, S. J. Oh, S. Chun, J. Choe, and Y. Yoo, “Cutmix: Regularization strategy to train strong classifiers with localizable features,” in *Proceedings of IEEE International Conference on Computer Vision (ICCV)*, 2019, pp. 6023–6032.
- [45] G. Ghiasi, Y. Cui, A. J. Srinivas, R. Qian, T.-Y. Lin, E. D. Cubuk, Q. V. Le, and B. Zoph, “Simple copy-paste is a strong data augmentation method for instance segmentation,” in *Proceedings of IEEE Conference on Computer Vision and Pattern Recognition (CVPR)*, 2021, pp. 2918–2928.
- [46] A. Xiao, J. Huang, D. Guan, K. Cui, S. Lu, and L. Shao, “Polarmix: A general data augmentation technique for lidar point clouds,” in *Advances in Neural Information Processing Systems (NeurIPS)*, 2022, pp. 11 035–11 048.
- [47] C.-Y. Lee, T. Batra, M. H. Baig, and D. Ulbricht, “Sliced wasserstein discrepancy for unsupervised domain adaptation,” in *Proceedings of IEEE Conference on Computer Vision and Pattern Recognition (CVPR)*, 2019, pp. 10 285–10 295.
- [48] B. Sun and K. Saenko, “Deep coral: Correlation alignment for deep domain adaptation,” in *Computer Vision—ECCV 2016 Workshops: Amsterdam, The Netherlands, October 8–10 and 15–16, 2016, Proceedings, Part III 14*. Springer, 2016, pp. 443–450.
- [49] T.-H. Vu, H. Jain, M. Bucher, M. Cord, and P. Pérez, “Advent: Adversarial entropy minimization for domain adaptation in semantic segmentation,” in *Proceedings of IEEE Conference on Computer Vision and Pattern Recognition (CVPR)*, 2019, pp. 2517–2526.



**Jaeyul Kim** received the B.S. degree in the Department of Mechanical and Automotive Engineering from Seoul National University of Science and Technology (SEOULTECH) in 2018, and the M.S. in the Automotive Engineering from SEOULTECH in 2021. He is currently pursuing the Ph.D. degree in Electrical Engineering and Computer Science at DGIST, Daegu, Korea. His research interests include computer vision, autonomous driving and sensor fusion.



**Jungwan Woo** received the B.S. degree in the School of Undergraduate Studies of Daegu Gyeongbuk Institute of Science & Technology (DGIST), Daegu, Korea, in 2019. Since then, he has been pursuing his Ph.D. in Electrical Engineering and Computer Science at the same institution. His research interests include 3D perception, robot vision, and robot navigation.



**Jeonghoon Kim** received the B.S. degree in from Daegu Gyeongbuk Institute of Science & Technology (DGIST) in 2019. He is currently pursuing the M.S. & Ph.D. degree in Electrical Engineering and Computer Science at DGIST from 2019. His research interests include computer vision, vision-language, and machine learning.



machine learning.

**Sunghoon Im** received the B.S. degree in the Department of Electronic Engineering from Sogang University in 2014, and the M.S. and Ph.D. degree in the School of Electrical Engineering from KAIST in 2016 and 2019. He joined the Department of Electrical Engineering and Computer Science at DGIST, Daegu, Korea, in 2019, where he is currently working as an associate professor. He was a recipient of Microsoft Research Asia fellowship and Global Ph.D. fellowship from NRF of Korea. His research interests include computer vision, robot vision, and